Observation of Double Weyl Phonons in Parity-Breaking FeSi

H. Miao,[1,*,‡] T. T. Zhang,[2,3,‡] L. Wang,[2,3,‡] D. Meyers,[1] A. H. Said,[4] Y. L. Wang,[1] Y. G. Shi,[2] H. M. Weng,[2,5] Z. Fang,[2,5] and M. P. M. Dean[1,†]

[1]*Condensed Matter Physics and Materials Science Department, Brookhaven National Laboratory, Upton, New York 11973, USA*
[2]*Beijing National Laboratory for Condensed Matter Physics, Institute of Physics, Chinese Academy of Sciences, Beijing 100190, China*
[3]*University of Chinese Academy of Sciences, Beijing 100049, China*
[4]*Advanced Photon Source, Argonne National Laboratory, Argonne, Illinois 60439, USA*
[5]*Collaborative Innovation Center of Quantum Matter, Beijing 100190, China*

(Received 27 April 2018; published 18 July 2018)

Condensed matter systems have now become a fertile ground to discover emerging topological quasiparticles with symmetry protected modes. While many studies have focused on fermionic excitations, the same conceptual framework can also be applied to bosons yielding new types of topological states. Motivated by Zhang *et al.*'s recent theoretical prediction of double Weyl phonons in transition metal monosilicides [Phys. Rev. Lett. **120**, 016401 (2018)], we directly measure the phonon dispersion in parity-breaking FeSi using inelastic x-ray scattering. By comparing the experimental data with theoretical calculations, we make the first observation of double Weyl points in FeSi, which will be an ideal material to explore emerging bosonic excitations and its topologically nontrivial properties.

DOI: 10.1103/PhysRevLett.121.035302

In crystalline materials, phonons are the most fundamental bosonic quasiparticle (QP) that are used to describe the collective motion of periodically distributed atoms. Inspired by the development of topological band theory on fermionic QPs [1–3], topological phonons have attracted extensive theoretical and experimental attention [4–18]. Previous studies of topological acoustic QPs have focused on artificial macroscopic mechanical systems in the kHz ($\sim 10^{-8}$ meV) energy range due to potential applications in phononic waveguides [4–17]. Very recently, topological phonons have been theoretically predicted to exist in natural crystalline materials MSi (M = Fe, Co, Mn, Re, Ru) [18]. These topological excitations are the fundamental QPs of the corresponding crystalline lattices and occur in the THz ($\sim$10 meV) energy range, in which phonons often play a dominant role in the thermal and electronic properties of solids. Here we use inelastic x-ray scattering (IXS) to perform the first experimental measurement of the THz topological phonon dispersion in parity-breaking crystalline FeSi. By directly tracking the bulk phonon dispersion near the high symmetry points, we demonstrate the existence of the theoretically predicted double Weyl points, which have not yet been observed experimentally in related Fermion systems. Our results thus establish transition metal monosilicides as new model systems to explore topological bosonic excitations and symmetry protected properties such as the topological nontrivial edge modes.

FeSi has the B20-type structure with noncentrosymmetric space group $P2_13$ (no. 198). As we show in Fig. 1(a), both Fe and Si atoms are located at the 4(a)-type site in the simple cubic unit cell with position coordinates (u, u, u), $(\frac{1}{2}+u, \frac{1}{2}-u, -u)$, $(-u, \frac{1}{2}+u, \frac{1}{2}-u)$, and $(\frac{1}{2}-u, -u, \frac{1}{2}+u)$, where $u_{\mathrm{Fe}} = 0.13652$ and $u_{\mathrm{Si}} = 0.8424$. Therefore, FeSi has three twofold screw rotations C'_{2i} ($i = x, y, z$) along each $\langle 100 \rangle$ axis (e.g., $\{C_{2x}|(\frac{1}{2}, \frac{1}{2}, 0)\}$ along the x axis) and one threefold rotation C_3 along the $\langle 111 \rangle$ axes. In reciprocal space, the particular crystal symmetry of FeSi gives

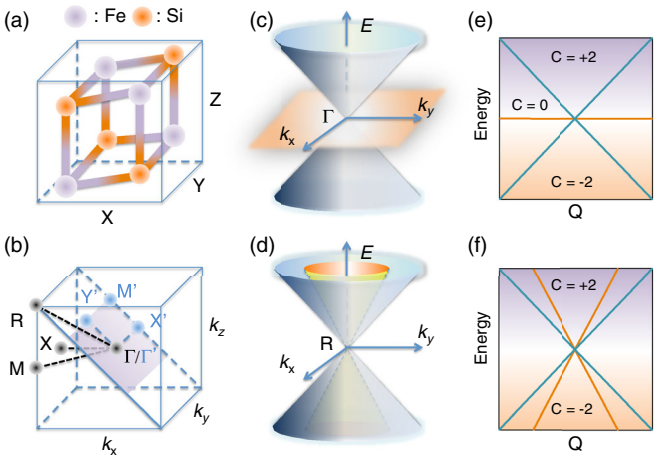

FIG. 1. Two types of double Weyl points are predicted in FeSi [18]. (a),(b) Cubic unit cell and the Brillouin zone (BZ) of FeSi, respectively. The purple (101) plane corresponds to the exposed sample surface in our measurement. The high symmetry points in the 3D BZ and the projected 2D BZ are shown in black and light blue, respectively. (c),(d) Schematic 3D view of the spin-1 Weyl point and charge-2 Dirac point, respectively. Their corresponding 2D view projections and Chern numbers are shown in (e),(f), respectively.

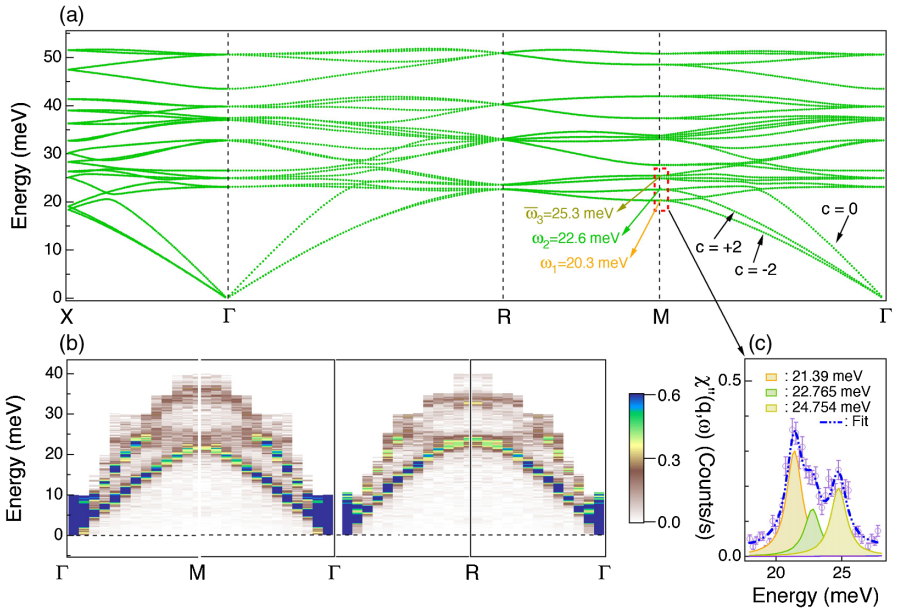

FIG. 2. Effective spin-1 Weyl acoustic phonons. (a) DFPT calculated phonon dispersion along the X-Γ-R-M-Γ direction. The Chern numbers for the longitudinal mode at higher energy and the two transverse modes at lower energy are 0 and ± 2, respectively. Because of the parity symmetry ($\mathcal{P}$) breaking in FeSi, the two transverse acoustic modes are split with the largest energy separation located in the red dashed square at the M point. (b) IXS measured phonon dispersion along the $M(4.5, 0.5, 0)$-$\Gamma(4, 0, 0)$-$R(4.5, 0.5, 0.5)$ direction. The dispersion along the Γ-M and R-Γ directions is symmetrized from the raw data with respect to the M and the R points, respectively. (c) High-statistic IXS data provide evidence for splitting of the two transverse acoustic phonons at the M point.

rise to threefold representations at the Brillouin zone (BZ) center (the Γ point) and fourfold representations at the BZ corner [the R point as shown in Fig. 1(b)] [18].

For spin-1/2 excitations that are relevant to fermionic electronic band dispersions, the Weyl point is usually described by the two-band Hamiltonian $H_2(\mathbf{k}) = (\hbar/2)\mathbf{k}\cdot\boldsymbol{\sigma}$. Here $\mathbf{k}$ and $\boldsymbol{\sigma}$ are the QP's momentum and Pauli's matrix, respectively. The corresponding Chern numbers of the two bands are $+1$ and -1, respectively. The effective Hamiltonian describing the Weyl points in the bosonic three- and four-band systems can be written as $H_3(\mathbf{q}) = (\hbar/2)\mathbf{q}\cdot\mathbf{L}$ and $H_4(\mathbf{q}) = \left(\begin{smallmatrix}\mathbf{q}\cdot\sigma & 0\\ 0 & \mathbf{q}\cdot\sigma\end{smallmatrix}\right)$, respectively. Here $\mathbf{q}$ is the reduced momentum transfer in the first Brillouin zone, which is defined as $\mathbf{q} = \mathbf{Q} - \mathbf{G}_n$, with $\mathbf{Q}$ and $\mathbf{G}_n$ representing the momentum transfer and reciprocal vector, respectively. $\mathbf{L}$ is the spin-1 matrix representation of the rotation generator. The Weyl points and the corresponding Chern numbers that are derived from the effective Hamiltonians $H_3(\mathbf{q})$ and $H_4(\mathbf{q})$ are thus dubbed the effective spin-1 Weyl point and the effective charge-2 Dirac point, respectively, both of which are special cases of double Weyl points [18].

In this Letter, we use high-resolution IXS to directly measure the acoustic effective spin-1 Weyl point and optical effective charge-2 Dirac points in a high-quality single crystal FeSi of approximately 2 mm × 3 mm × 120 μm. The experiments were conducted at beam line 30-ID-C (high energy resolution inelastic x-ray scattering [19,20]) at the Advanced Photon Source. The highly monochromatic x-ray beam of incident energy $E_i = 23.7$ keV ($\lambda = 0.5226$ Å) was focused on the sample with a beam cross section of $\sim 35 \times 15$ μm^2 (horizontal × vertical). The total energy resolution of the monochromatic x-ray beam and analyzer crystals was $\Delta E \sim 1.5$ meV (full width at half maximum). The measurements were performed in transmission geometry. Typical counting times were in the range of 30 to 120 s per point in the energy scans at constant momentum transfer $\mathbf{Q}$.

We first focus on the effective spin-1 Weyl acoustic phonons. Figure 2a shows the phonon band structure along the X-Γ-R-M-Γ direction calculated using the VIENNA *AB INITIO* SIMULATION PACKAGE [21] and the density functional perturbation theory (DFPT) [22] with fully relaxed lattice parameters $a = b = c = 4.373$ Å. The generalized gradient approximation was used for the exchange-correlation function [23]. We note that phonons in FeSi will be generally softened when increasing the temperature or when including spin-phonon interactions [24]. Since our calculations were done for the nonmagnetic ground state at zero temperature, a rescaled factor of 0.85 in energy was used to directly compare the IXS data, which was performed at room temperature. We note that this scaling is larger than one expects and may reflect an incomplete description of the strong correlations in FeSi [24]. Although the three branched acoustic phonon is a generic feature of three-dimensional systems, as we show in Fig. 2(a), the Chern numbers of the two transverse acoustic modes are well defined only when they are separated from

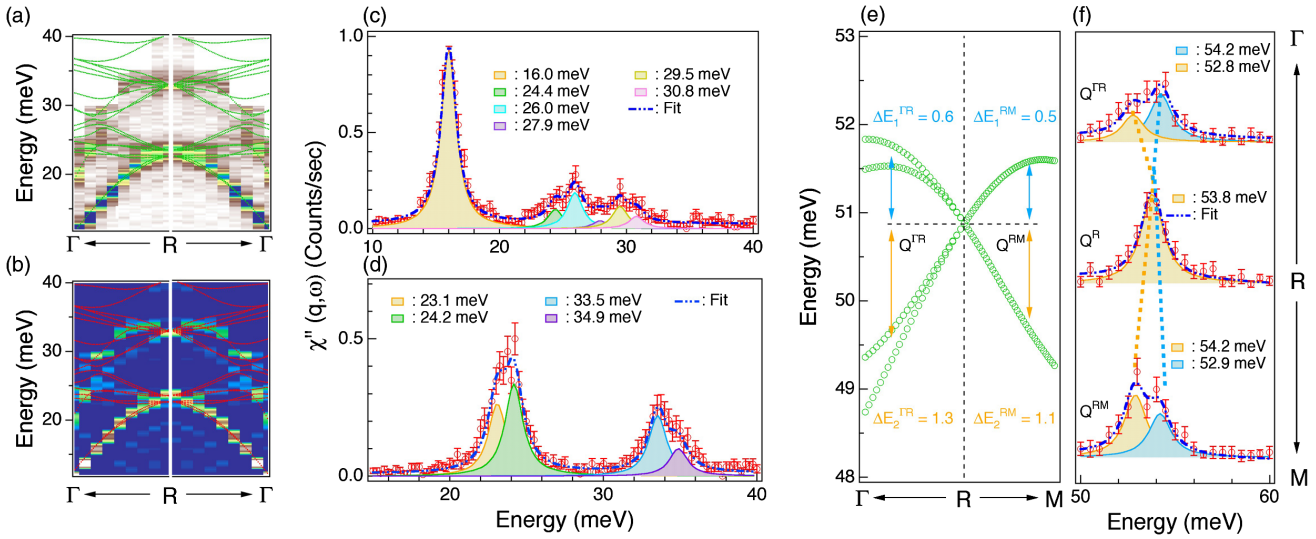

FIG. 3. Effective charge-2 Dirac points. (a),(b) Phonon dispersion and its second derivative plot near the R point. The green and red curves are the same rescaled DFPT calculations. High-statistic IXS spectra at $\mathbf{Q} = (4.26, 0.26, 0.26)$ and (4.5,0.5,0.5) are shown in (c), (d), respectively. The dashed blue curves are the fitted result. The number of phonon peaks in the fitting is based on the DFPT calculation (see the Supplemental Material [25]). (e) Rescaled phonon dispersion near the high-energy effective charge-2 Dirac point. The high-statistic IXS spectra at $\mathbf{Q}^{\Gamma R}$, $\mathbf{Q}^{R}$, and $\mathbf{Q}^{RM}$ are shown in (f). The peak positions extracted from the IXS spectra are slightly higher than the rescaled DFPT calculation, suggesting different rescale factors for the low- and high-energy phonons.

each other, which can only happen if the parity symmetry $\mathcal{P}$ or the time reversal symmetry $\mathcal{T}$ is broken [18]. Figure 2(b) shows the phonon dispersion along the M-Γ-R direction at room temperature. In agreement with the DFPT calculation, the transverse and longitudinal acoustic modes are well separated along both the Γ-M and Γ-R directions. To prove the two transverse acoustic modes are indeed separated, we performed high-statistics IXS measurement at the M point (4.5,0.5,0), where the energy difference is predicted to be the largest in the entire BZ. The data are shown in the energy window between 18 and 28 meV, which corresponds to the red dashed squares shown in Fig. 2(a). Three nondegenerate modes are observed in the experimental data that correspond to the well-separated transverse acoustic modes and the two nearly degenerate optical modes near 25.3 meV. The IXS spectra were fitted to the standard damped harmonic oscillator functions [25–28]. The results are shown in Fig. 2(c) and reveal good consistency with the DFPT calculation.

Having the effective spin-1 Weyl acoustic phonons established, we now turn to the effective charge-2 Dirac points at the R point. The generating elements of the little group at the R point are the rotation symmetry C_3, the screw rotation symmetry $\{C_{2x}|(\frac{1}{2}, \frac{1}{2}, 0)\}$, and the time-reversal symmetry $\mathcal{T}$. The symmetry analysis has proven that the minimal representation is four-dimensional with $\mathcal{T}$-protected Chern numbers ± 2 [18]. Here we first look at the charge-2 Dirac points below 40 meV. Figure 3(a) displays the phonon dispersion near the R point. Its second derivative shown in Fig. 3(b) enables a better visibility of the dispersion that allows direct comparison of the results with the DFPT calculation. The experimentally determined dispersion is in good agreement with the DFPT calculation and resolves both the multiple Charge-2 Dirac points at the R point and the band hybridization along the Γ-R direction. To quantitatively determine the band hybridization and the energy of charge-2 Dirac points, we fit the long counting time IXS spectra at $\mathbf{Q} = (4.26, 0.26, 0.26)$ and the R point [see Figs. 3(c) and 3(d) [25]]. The fitted results are consistent with the DFPT calculation and reveal four charge-2 Dirac points between 20 and 40 meV.

We now move to the high-energy charge-2 Dirac point at the R point. Since the phonon structure factor $S(q, \omega)$ is proportional to $1/\omega_q$, where ω_q is the phonon energy, we restricted our measurements to $\mathbf{Q}^{\Gamma R}$, $\mathbf{Q}^{R}$, and $\mathbf{Q}^{RM}$ shown in Fig. 3(f). Based on the DFPT calculation shown in Fig. 3(e), the single phonon peak at $\mathbf{Q}^{R}$ is predicted to separate into two and four peaks at $\mathbf{Q}^{RM}$ and $\mathbf{Q}^{\Gamma R}$, respectively. However, due to the small energy difference and the finite equipment resolution, two resolution limited peaks are expected to be observed at both $\mathbf{Q}^{RM}$ and $\mathbf{Q}^{\Gamma R}$. This is indeed what we observed in Fig. 3(f): the resolution limited peak at $\mathbf{Q}^{R}$ and $\omega_R = 53.8$ meV splits into two resolution limited peaks at $\mathbf{Q}^{\Gamma R/RM}$ and $\omega_{\text{up}}^{\Gamma R/RM} = 54.2/54.2$ meV and $\omega_{\text{down}}^{\Gamma R/RM} = 52.8/52.9$ meV and, hence, confirms the high-energy charge-2 Dirac point.

The existence of spin-1 Weyl points at the Γ point and the charge-2 Dirac points at the R point will give rise to topologically nontrivial edge modes, which cannot be continuously deformed into an even number of noncontractable loops wrapping around the BZ torus. Since x rays have a

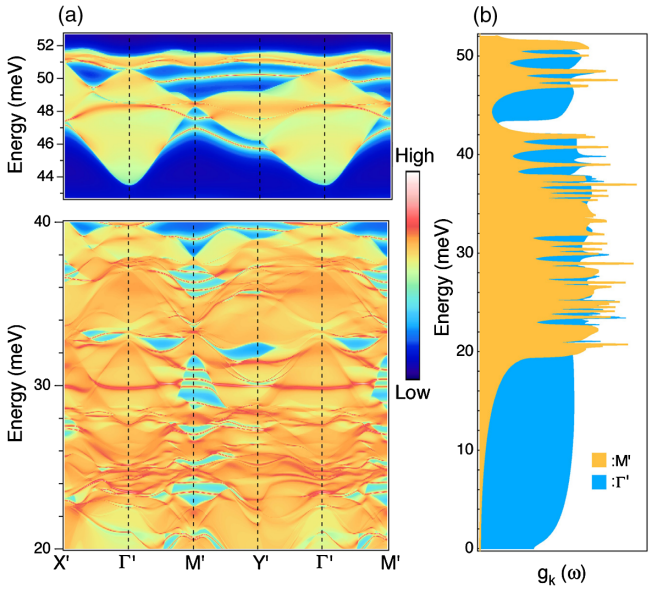

FIG. 4. Topological surface modes. (a) Momentum resolved phonon dispersion projected on the (110) surface. The definition of the surface high symmetry points is shown in Fig. 1(b). (b) Phonon DOS at the surface M' and Γ' points. The high surface DOS at the M' point makes this point the best place to identify topological edge modes.

penetration depth of a few microns, IXS has minimal sensitivity to the topological phonon modes on the surface. Here, we calculate the (110) surface phonon band structure by constructing the surface Green's function [18,29–31]. Because of the presence of the phonon band gap around 42 meV, the surface states that correspond to the high-energy double Weyl points are well separated from the bulk band structure through the entire BZ and form a noncontractable Fermi arc around 50 meV. In contrast, the surface states between 20 and 40 meV are largely overlapping with the bulk band structure making it difficult to be experimentally separated away from the M' point. This can be better visualized in Fig. 4(b), where the surface phonon density of states (DOS) $g_{M'}(\omega)$ and $g_{\Gamma'}(\omega)$ are shown at the surface M' and the Γ' point. The calculation at the M' point reveals that spikes that correspond to large surface phonon DOS are well separated from the broad continuum, while at the Γ' point the surface DOS is dominated by the broad continuum. Since the phonon intensity is much larger at low energy, the theoretically predicted high surface phonon DOS between 20 and 40 meV at the surface M' point makes the topological edge modes easier to be identified by surface sensitive probes such as electron energy loss spectroscopy and helium scattering.

In summary, using IXS and theoretical calculations on parity-breaking FeSi, we report the first experimental observation of phonon double Weyl points. Our results thus establish transition metal monosilicides as new model systems to explore emerging quantum excitations and imply the existence of topological nontrivial edge modes based on the symmetry propagation of the bulk modes.

H. M. and M. P. M. D. acknowledge A. Alexandradinata, C. Fang, L. Lu, and D. Mazzone for insightful discussions. This material is based upon work supported by the U.S. Department of Energy, Office of Basic Energy Sciences, Early Career Award Program under Award No. 1047478. Work at Brookhaven National Laboratory was supported by the U.S. Department of Energy, Office of Science, Office of Basic Energy Sciences under Contract No. DE-SC0012704. The IXS experiments were performed at 30ID in the Advanced Photon Source, a U.S. Department of Energy (DOE) Office of Science User Facility operated for the DOE Office of Science by Argonne National Laboratory under Contract No. DE-AC02-06CH11357. We acknowledge the support from the National Key Research and Development Program of China (Grant No. 2016YFA0300600), the National Natural Science Foundation of China (Grants No. 11674369 and No. 11774399), and the Chinese Academy of Sciences (XDB07020100 and QYZDB-SSW-SLH043).

*hmiao@bnl.gov
†mdean@bnl.gov
‡These authors contributed equally to this work.

[1] M. Z. Hasan and C. L. Kane, Rev. Mod. Phys. **82**, 3045 (2010).
[2] X.-L. Qi and S.-C. Zhang, Rev. Mod. Phys. **83**, 1057 (2011).
[3] N. P. Armitage, E. J. Mele, and A. Vishwanath, Rev. Mod. Phys. **90**, 015001 (2018).
[4] E. Prodan and C. Prodan, Phys. Rev. Lett. **103**, 248101 (2009).
[5] C. L. Kane and T. C. Lubensky, Nat. Phys. **10**, 39 (2014).
[6] B. G.-g. Chen, N. Upadhyaya, and V. Vitelli, Proc. Natl. Acad. Sci. U.S.A. **111**, 13004 (2014).
[7] Z. Yang, F. Gao, X. Shi, X. Lin, Z. Gao, Y. Chong, and B. Zhang, Phys. Rev. Lett. **114**, 114301 (2015).
[8] P. Wang, L. Lu, and K. Bertoldi, Phys. Rev. Lett. **115**, 104302 (2015).
[9] M. Xiao, W.-J. Chen, W.-Y. He, and C. T. Chan, Nat. Phys. **11**, 920 (2015).
[10] L. M. Nash, D. Kleckner, A. Read, V. Vitelli, A. M. Turner, and W. T. M. Irvine, Proc. Natl. Acad. Sci. U.S.A. **112**, 14495 (2015).
[11] R. Süsstrunk and S. D. Huber, Science **349**, 47 (2015).
[12] S. H. Mousavi, A. B. Khanikaev, and Z. Wang, Nat. Commun. **6**, 8682 (2015).
[13] R. Süsstrunk and S. D. Huber, Proc. Natl. Acad. Sci. U.S.A. **113**, E4767 (2016).
[14] J. Lu, C. Qiu, L. Ye, X. Fan, M. Ke, F. Zhang, and Z. Liu, Nat. Phys. **13**, 369 (2017).
[15] C. He, X. Ni, H. Ge, X.-C. Sun, Y.-B. Chen, M.-H. Lu, X.-P. Liu, and Y.-F. Chen, Nat. Phys. **12**, 1124 (2016).
[16] R. Fleury, A. B. Khanikaev, and A. Alù, Nat. Commun. **7**, 11744 (2016).
[17] S. D. Huber, Nat. Phys. **12**, 621 (2016).
[18] T. Zhang, Z. Song, A. Alexandradinata, H. Weng, C. Fang, L. Lu, and Z. Fang, Phys. Rev. Lett. **120**, 016401 (2018).

[19] A. H. Said, H. Sinn, and R. Divan, J. Synchrotron Radiat. **18**, 492 (2011).
[20] T. S. Toellner, A. Alatas, and A. H. Said, J. Synchrotron Radiat. **18**, 605 (2011).
[21] G. Kresse and J. Furthmüller, Phys. Rev. B **54**, 11169 (1996).
[22] X. Gonze and C. Lee, Phys. Rev. B **55**, 10355 (1997).
[23] S. Baroni, S. de Gironcoli, A. Dal Corso, and P. Giannozzi, Rev. Mod. Phys. **73**, 515 (2001).
[24] S. Krannich, Y. Sidis, D. Lamago, R. Heid, J.-M. Mignot, H. v. Löhneysen, A. Ivanov, P. Steffens, T. Keller, L. Wang, E. Goering, and F. Weber, Nat. Commun. **6**, 8961 (2015).
[25] See Supplemental Material at http://link.aps.org/supplemental/10.1103/PhysRevLett.121.035302 for inelastic x-ray scattering cross section, spectra fittings, and sample growth.
[26] H. Miao, D. Ishikawa, R. Heid, M. Le Tacon, G. Fabbris, D. Meyers, G. D. Gu, A. Q. R. Baron, and M. P. M. Dean, Phys. Rev. X **8**, 011008 (2018).
[27] A. Q. Baron, arXiv:1504.01098v2.
[28] B. Fåk and B. Dorner, Physica (Amsterdam) B **234**, 1107 (1997).
[29] M. P. L. Sancho, J. M. L. Sancho, and J. Rubio, J. Phys. F **14**, 1205 (1984).
[30] M. P. L. Sancho, J. M. L. Sancho, J. M. L. Sancho, and J. Rubio, J. Phys. F **15**, 851 (1985).
[31] Q. Wu, S. Zhang, H.-F. Song, M. Troyer, and A. A. Soluyanov, Comput. Phys. Commun. **224**, 405 (2018).